22nd International Conference on Sustainable Energy Technologies
Kuala Lumpur, Malaysia, 13 to 15 August 2026 · ISBN 978-1-995850-00-9 · ISSN 2978-4387

CONFERENCE PAPER · AI & RENEWABLE SYSTEMS

Numerical investigation of the aeroelastic performance of a wind turbine operating under yaw misalignment

Shine Win Naung[1*], Summer Pimm[1], Kai Zhang[2], Yufeng Yao[1], Jun Yao[1], Mohammad Rahmati[3]

[1] School of Engineering, The University of the West of England, Bristol BS16 1QY, United Kingdom
[2] School of Ocean and Civil Engineering, Shanghai Jiao Tong University, Shanghai 200240, China
[3] School of Engineering, Physics and Mathematics, Northumbria University, Newcastle upon Tyne NE1 8ST, United Kingdom

RECEIVED 15 February 2026 · REVISED 21 March 2026 · ACCEPTED 28 March 2026
PRESENTED 13 to 15 August 2026 · PUBLISHED 23 November 2026

ABSTRACT

This paper presents a comprehensive aeroelastic analysis of a wind turbine rotor operating under yaw misalignment conditions, which are often overlooked in the literature despite their increasing application in wake-steering strategies. The primary objective is to investigate the coupled aerodynamic–structural interactions that influence rotor performance under yaw angles of 0°, 10°, 20°, and 30°, with particular emphasis on pressure distribution, blade deformation, dynamic force response, and potential risks associated with yaw control. A validated numerical framework combining Computational Fluid Dynamics (CFD) and Finite Element Analysis (FEA) is employed, followed by aeroelastic simulations incorporating blade vibration phase angles of 0° and 120°. The results reveal that yaw misalignment significantly affects blade aerodynamics and wake development, producing increased wake asymmetry and lateral deflection as the yaw angle increases. Structural analysis shows that yawed inflow generates non-uniform blade loading, resulting in asymmetric deformation and stress distributions. The maximum blade-tip deflection of 21.826 mm (1.07%R), where R is the rotor radius, occurs at 10° yaw, while the minimum deflection of 17.824 mm (0.874%R) is observed at 30° yaw. Aeroelastic simulations indicate that a 30° yaw angle introduces amplitude-modulated loading, reduces mean aerodynamic forces, and generates more complex rotating hub moments when combined with a 120° inter-blade vibration phase shift. Wall work density analysis suggests an overall stabilising aerodynamic damping effect, although the aeroelastic energy transfer is concentrated primarily near the blade-tip region. Furthermore, wake visualisation reveals enhanced flow unsteadiness, distorted helical tip vortices, and accelerated vortex breakdown at higher yaw angles. These findings highlight the importance of accounting for coupled aerodynamic, structural, and wake interactions when implementing yaw-steering strategies for wind farm power optimisation.

KEYWORDS Aeroelasticity, Aerodynamics, Fluid-structure interaction, Wind turbine, Energy, Turbomachinery

1. Introduction

The Global Wind Report 2025 highlights a record-breaking year in 2024, with 117 GW of new wind power installations worldwide (Global Wind Energy Council 2025). This raises the global cumulative wind energy capacity to 1,136 GW, with top markets in China, US, Brazil, India and Germany. Currently, the UK has an onshore wind operational capacity of approximately 15.9 GW and an offshore capacity of around 16 GW. Combined, these installations could generate enough electricity to power about 26.5 million homes. It is estimated that nearly 2.5 GW of floating offshore power could be operational by 2030. Floating offshore wind turbines, deployed in deeper waters to access high and

* Corresponding author. Email address: Shine.WinNaung@uwe.ac.uk (Shine Win Naung)

© 2026 The Author(s).
Published by Caravel Press.

doi.org/10.65582/set.2026.030

steady wind resources, have become more significant for future power generation from offshore wind (RenewableUK 2024).

With the rapid growth of offshore wind farms, the optimisation of wind farm layout has become increasingly crucial for maximising energy yield and minimising wake losses. Numerous studies have examined various strategies to improve aerodynamic performance. (Win Naung *et al.* 2021c) conducted a numerical analysis of two wind turbines in an in-line configuration and concluded that the distance between the upstream and downstream wind turbines in a wind farm should be a minimum of 5 rotor diameters. (Shao *et al.* 2025) developed an effective wind farm layout optimisation framework using a Kriging model, that could reduce the computation time significantly. Recent studies such as (Yang *et al.* 2021) suggested that the deliberate yaw misalignment of upstream wind turbines which redirects wake flows could enhance power generation of downstream turbines, thereby increasing overall power generation from a wind farm. (Tu *et al.* 2023) proposed a yaw-control strategy for an optimisation of power generation from two tandem wind turbines and argued that an appropriate yaw misalignment of wind turbines could improve the average energy production in a wind farm. These approaches have demonstrated promising results in overall power generation efficiency; however, the complex interactions between the unsteady flow and the turbine structure are often overlooked. Uneven aerodynamic loading, structural responses, and long-term reliability would pose significant risks to turbine integrity and operational costs. (Hansen 2007) highlighted the increased risk of aeroelastic instabilities, including stall-induced vibration and flutter, resulting from the growing size and length of modern offshore wind turbine blades. Therefore, it is important to develop a holistic approach that integrates aerodynamic benefits with structural integrity to ensure sustainable and cost-effective offshore wind development.

The aeroelastic behaviour of wind turbines arises from the interaction between aerodynamic forces and structural flexibility, that requires integrated modelling approaches to predict blade deformation under different operating conditions. A commonly adopted technique for aerodynamic load estimation is the Blade Element Momentum (BEM) method, which combines blade element theory with momentum principles to deliver a computationally efficient framework for performance analysis as discussed in (Abdelkhalig *et al.* 2022). In this approach, the rotor blade is partitioned into a set of discrete sections, and local flow conditions are used to compute aerodynamic forces. Extensions of the BEM framework have been proposed to address nonlinear effects; for instance, (Wang *et al.* 2014) developed a nonlinear aeroelastic modelling to consider large deflections in wind turbine blades, while (Fernandez *et al.* 2018) integrated aero-structural coupling for improved modelling fidelity. Despite its widespread use, the BEM method is still constrained by the assumptions of quasi-steady aerodynamics and simplified wake representation, which limit its ability to capture transient phenomena such as dynamic stall or complex wake interactions. To mitigate these limitations, empirical corrections are often introduced as discussed by (Boatto *et al.* 2023). However, the reliability of the method is still limited for highly unsteady or strongly coupled aeroelastic scenarios.

To overcome the inherent limitations of the BEM-based approaches, advanced vortex models have been introduced to better represent wake dynamics. These models generally fall into two categories: free-wake and prescribed-wake formulations as highlighted in (Lee *et al.* 2022). Free-wake techniques explicitly track the evolution of shed wake vortices to enable a detailed and time-dependent description of wake behaviour, whereas prescribed-wake methods impose simplified, pre-defined wake geometries to reduce complexity of wake motions. Free-wake models have been applied to investigate aerodynamic and aeroelastic responses of turbine blades under different operating conditions (Rodriguez and Jaworski 2020), while prescribed-wake implementations, such as lifting-line theory, have been used to study phenomena such as stall delay (Breton *et al.* 2008). In addition to vortex methods, actuator-based methods are also widely employed for wind turbine aerodynamic modelling. Actuator-based approaches such as actuator disk and actuator line models approximate the rotor or the blade as distributed momentum sources, thus simplifying the flow field while

preserving global aerodynamic effects, as discussed in (Arabgolarcheh *et al.* 2022). These actuator models are typically integrated with flow solvers that resolve the Navier–Stokes equations to capture wake development, as explained in (Wang *et al.* 2024). While actuator methods provide high-resolution representation of wake dynamics and interactions for large-scale wind farm simulations, the computational costs of these simulations can still be significant. Despite improved physical fidelity compared to the BEM models, their accuracies often rely on BEM-derived load inputs at a significantly higher computational cost (O'Brien *et al.* 2017).

Computational Fluid Dynamics (CFD) provides a high-fidelity framework for analysing wind turbine aerodynamics, with detailed resolution of complex flow fields and turbulence around rotor blades. A CFD model can accurately predict aerodynamic loads and capture transient flow phenomena such as dynamic stall and wake interactions, provided that turbulence modelling is appropriately applied (Zhang *et al.* 2024). For aeroelastic studies, these aerodynamic predictions are coupled with structural solvers through fluid–structure interaction (FSI) techniques. For instance, (Wang *et al.* 2016) combined CFD with a Finite Element Analysis (FEA) model to examine stress distribution and blade deflection, while (Dai *et al.* 2017) explored aeroelastic performance under varying yaw conditions. Similarly, (Dose *et al.* 2018; Dose *et al.* 2020) implemented coupled CFD–Computational Structural Dynamics (CSD) approaches to resolve time-dependent aerodynamic and structural responses.

With the increasing size and flexibility of wind turbine blades, aeroelastic stability has become a critical design consideration and emerged as a major focus in current research efforts. Recently, nonlinear frequency-domain formulations have been applied to wind turbine aeroelastic modelling to predict the aeroelastic stability of the blades under different flow conditions, as discussed by (Win Naung *et al.* 2025a). (Howison *et al.* 2018) and (Drofelnik *et al.* 2018) employed Navier–Stokes-based Harmonic Balance Method (HBM) models to predict flutter with high accuracy at a reduced computational cost compared to time-domain CFD simulations. More recently, (Horcas *et al.* 2017) and (Win Naung *et al.* 2021d) extended these approaches to large-scale wind turbines and showed that frequency-domain formulations can capture aerodynamic damping and stability characteristics efficiently. These methods approximate unsteady periodic responses by expressing flow variables as harmonic components, thus significantly reducing computational effort compared to time-domain transient simulations. However, its predictive accuracy depends on the appropriate selection of structural modes, vibration frequencies, and the number of harmonics considered. Furthermore, (Win Naung *et al.* 2021b) highlighted that the unsteady inflow conditions have a great impact on the distribution of the aerodynamic loads on the blades, and thereby affecting the aeroelastic stability.

This study aims to investigate the aeroelastic characteristics of a wind turbine operating under yaw misalignment conditions, that has received limited attention in the recent literature. A high-fidelity unsteady CFD model will be employed to compute aerodynamic loads, together with a transient FEA model for structural responses, to provide a comprehensive assessment of blade behaviour at different yaw angles. Several yaw angles of 0°, 10°, 20° and 30° will be considered. The objective is to conduct a detailed aeroelastic analysis that captures the coupled aerodynamic–structural interactions influencing turbine stability and performance. This includes quantifying stress distribution across blades, measuring deformation patterns under varying yaw angles, and evaluating unsteady behaviour over several vibration cycles. By identifying how these factors vary under yaw misalignment, the study will highlight potential structural risks such as increased aerodynamic loading, non-uniform dynamic responses, and amplified stress ranges, which could impact long-term reliability and operational safety of the turbine.

2. Physical description

For the numerical simulations in this study, the well-established MEXICO (Model Rotor Experiments in Controlled Conditions) wind turbine benchmark model, as explained in (Schepers *et al.* 2014; Snel *et al.* 2007), is adopted. The rotor consists of three blades with a diameter of 4.5 m and individual

blade length of 2.04 m. Simulations are performed at a wind speed of 15 m/s, rotational speed of 424.5 RPM, and a blade pitch angle of −2.3°. Further details of the MEXICO configuration are available in (Schepers *et al.* 2014; Snel *et al.* 2007), and previous applications of this model by the authors can be found in (Win Naung *et al.* 2025b; Win Naung *et al.* 2025a). As used in the experiment, the blade is made of an aluminium alloy which possesses a density of 2770 kg/m^3, a Young's modulus of 7.10×10^{10} Pa, and a Poisson ratio of 0.27, respectively. Additionally, the study examines the effects of yaw misalignment at different yaw angles including 0°, 10°, 20° and 30°, as illustrated in Fig. 1.

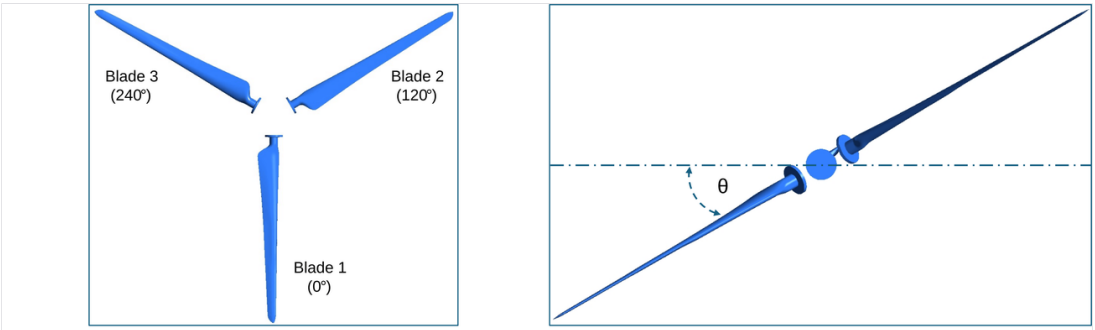

a) MEXICO rotor model **b)** Yaw angle configuration

Figure 1. MEXICO rotor model and yaw angle configuration.

3. Methodology

3.1. CFD modelling

3.1.1. Governing equations

A pressure-based, finite volume solver (ANSYS CFX 2024 R2) is used for the CFD modelling, and the Navier-Stokes equations in a general Cartesian coordinate system are given by:

$$\frac{\partial}{\partial t}\int_V U dV + \int_A \vec{F}_I . d\vec{A} + \int_A \vec{F}_V . d\vec{A} = \int_V S dV \tag{1}$$

In the above equation, V is the volume, and A is the surface. U is the vector of the conservative variables. $\vec{F}_I$ and $\vec{F}_V$ are respectively the inviscid and viscous flux vectors. S contains the source terms. Reynolds-averaged Navier Stokes (RANS) model is employed in this study, where the k-ω SST (shear stress transport) model (Menter *et al.* 2003) is used for turbulence modelling to enhance the prediction of separated flows.

3.1.2. Computational domain and mesh

The computational setup consists of a stationary outer domain and a rotating sub-domain to model rotor motion, connected through a transient rotor–stator sliding interface to accurately capture unsteady flow interactions. A full 360° model of the rotor, including all three blades, is employed to represent the complete 3D geometry features. The rotating sub-domain can be rotated to introduce the yaw angle for yaw misalignment simulations. The computational domain extends 5R upstream, 15R downstream, an inlet diameter of 10R and an outlet diameter of 20R (where R is the rotor radius) of the rotor plane to ensure sufficient space for modelling external flow (see Fig. 2a). The mesh is generated with an unstructured grid within a conical domain designed to accommodate wake expansion in the downstream region. Local mesh refinement is applied around blade surfaces and in the wake region, with 20 inflation layers at a growth rate of 1.2 to maintain $y^+ < 1$ for the first layer height to accurately resolve the near wall flow. The final mesh comprises approximately 28×10^6 cells

to provide adequate resolution for capturing aerodynamic loads and wake dynamics. The representative meshes are shown in Figs. 2b-2d, respectively.

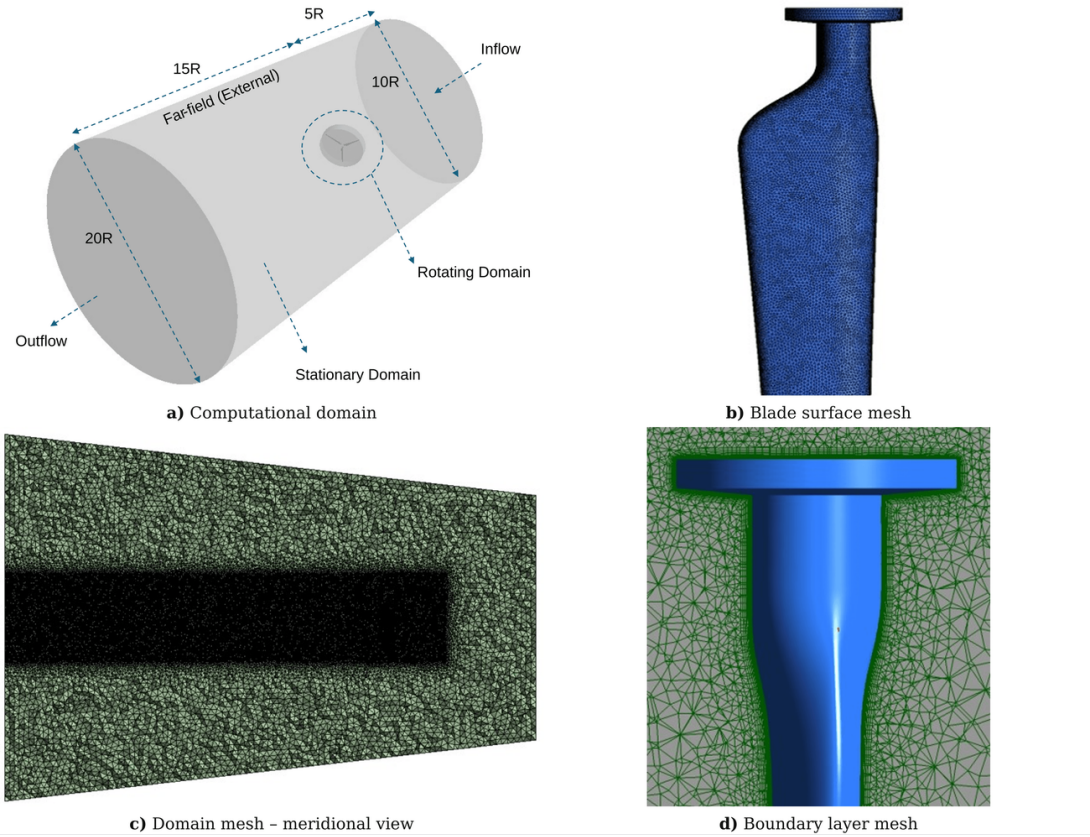

Figure 2. Computational domain and mesh of the CFD model.

3.1.3. Boundary conditions and numerical schemes

Uniform inflow conditions (i.e., wind speed and directions) are prescribed at the inlet and external far-field boundaries. A pressure outlet boundary is applied at the outlet. The blade surfaces are treated as no-slip adiabatic walls. The stationary outer domain and the rotating inner sub-domain are connected through a transient rotor–stator interface where interpolations are performed. Spatial discretisation employs a second-order upwind scheme, and temporal discretisation uses a second-order backward Euler method.

3.2. FEA modelling

3.2.1. Governing equations

The structural analysis is performed using an FEA solver (ANSYS Mechanical 2024 R2). The structural behaviour of the blade is governed by the following equations.

$$[M]\frac{\partial^2 \vec{d}}{\partial t^2} + [C]\frac{\partial \vec{d}}{\partial t} + [K]\vec{d} = \vec{f} \tag{2}$$

where, *[M]* is the mass matrix, *[C]* is the damping matrix, and *[K]* is the stiffness matrix. $\vec{f}$ is the total external load vector, which now includes the aerodynamic loads mapped from CFD solutions. In the FEA analysis, the aerodynamic load is imported from the CFD simulation as a pressure load applied to the blade surface, and structural responses are computed over several oscillation cycles.

3.2.2. Computational domain and mesh

The structural analysis of the wind turbine blade is performed using a three-dimensional finite element mesh composed of tetrahedral elements. This choice is driven by the blade's complex geometry, which makes tetrahedral meshing more suitable for conforming to highly curved surfaces compared to structured hexahedral meshes. The mesh utilises quadratic tetrahedral elements (10-node) to improve accuracy in stress and displacement predictions. Higher-order elements are selected to reduce data interpolation errors and better capture the blade's curvature without excessively increasing the element count. Mesh quality is evaluated using skewness metrics. The average skewness is maintained below 0.25, which is within recommended limits to ensure numerical stability. The FEA mesh consists of approximately 3×10^5 elements (see Fig. 3).

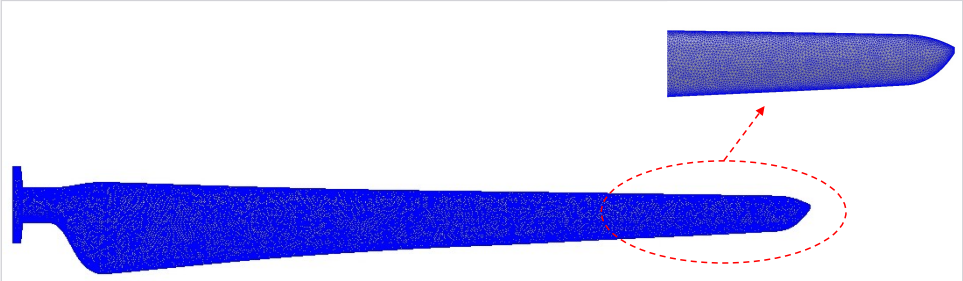

Figure 3. Computational mesh of the FEA model.

3.2.3. Boundary conditions and numerical schemes

The structural analysis is performed in a three-dimensional FEA domain. The blade root is fully constrained to replicate its rigid attachment to the hub, while aerodynamic pressure loads obtained from the CFD analysis are applied to the blade surfaces. Gravity and centrifugal forces are also included in the total external load vector term to account for the blade's self-weight and the desired rotational speed of 424.5 RPM. The analysis employs a transient solution method with nonlinear geometric effects activated. The solver uses a Newton–Raphson procedure, which iteratively updates the stiffness matrix at each load step to ensure equilibrium under nonlinear conditions, with a convergence tolerance of 1×10^{-8} to ensure numerical stability and accuracy.

3.3. Fluid-structure interaction

This work employs a pressure-based finite volume CFD solver, considering different yaw angles to assess the impact of yaw misalignment on the aeroelastic performance of a wind turbine rotor. The present study consists of two distinct stages. The first stage is a one-way fluid-structure interaction (FSI) analysis, in which the aerodynamic pressure loads computed by CFD are transferred to the FEA model to determine blade deformation, stress distribution, vibration frequencies, and vibration amplitudes. This stage is referred to as a one-way FSI analysis.

The second stage extends beyond a conventional one-way FSI calculation. The blade deformation and vibration characteristics obtained from the FEA analysis are subsequently used to prescribe blade motion in the CFD-based aeroelastic simulations. This approach is typically used in blade flutter analyses in turbomachinery applications. In these simulations, the dynamically moving blade is incorporated into the aerodynamic flow simulations to investigate the interaction between the unsteady flow and the blade structure vibration. This part of the analysis is referred to as the aeroelastic simulation in this paper. The aeroelastic response is computed using a time-domain CFD solution method. A schematic representation of the methodology is provided in Fig. 4.

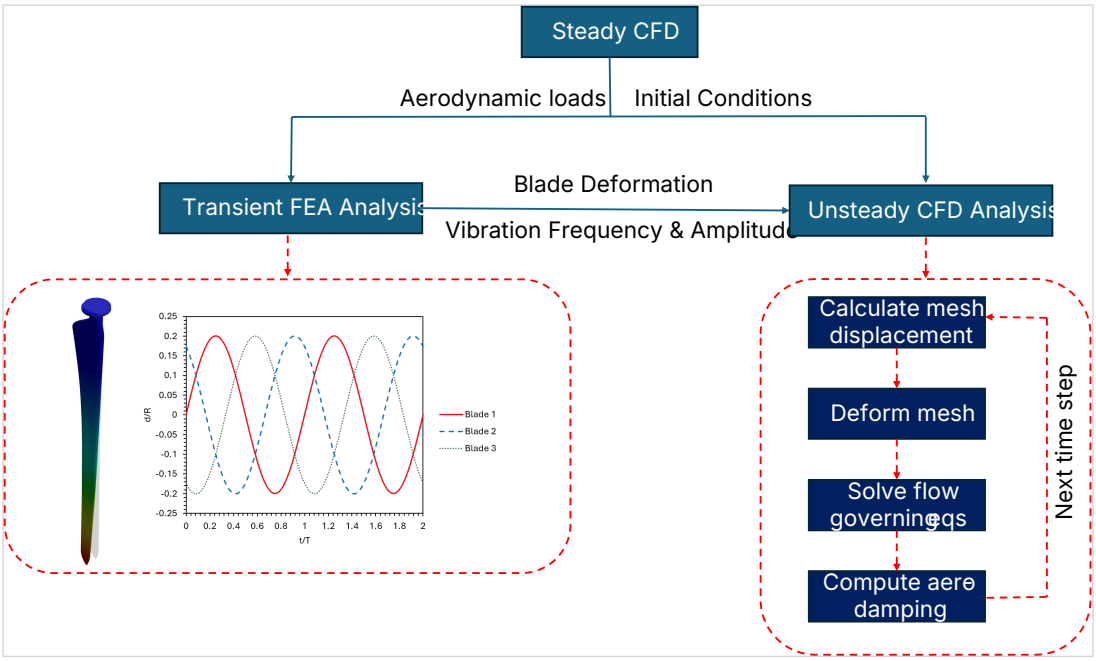

Figure 4. Fluid-structure interaction modelling flow chart.

4. Results and discussions

To assess the reliability of the numerical model, the time-averaged pressure coefficients C_p are extracted at several blade-span locations and compared with experimental measurements reported by (Snel *et al.* 2007). For additional validation, results from a benchmark simulation available in the literature (Bechmann *et al.* 2011) are also incorporated. This analysis demonstrates a strong agreement between the numerical predictions and experimental data. The comparative results at two spanwise locations (60% and 82% span) are only illustrated in Fig. 5 to make the paper concise.

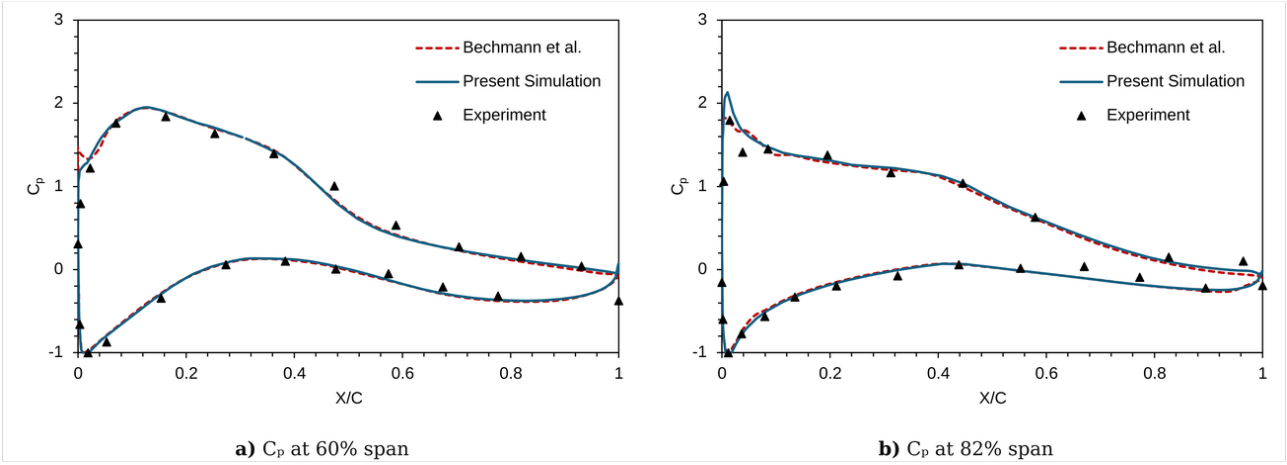

Figure 5. Time-averaged pressure coefficient distributions over the blade at different spanwise sections, computed by the present simulation, the reference simulation available in the literature, and the experiment.

Figure 6 shows the time-averaged pressure coefficients C_p extracted at 60% blade span for the 0° yaw angle (baseline) case and all other three yaw misalignment cases. It can be observed that, whilst the pressure coefficients are similar, especially beyond 0.6 *X/C*, the effect on the pressure coefficient is particularly apparent in the 30° case where the C_p on each side of the blade decreases considerably compared to the baseline case.

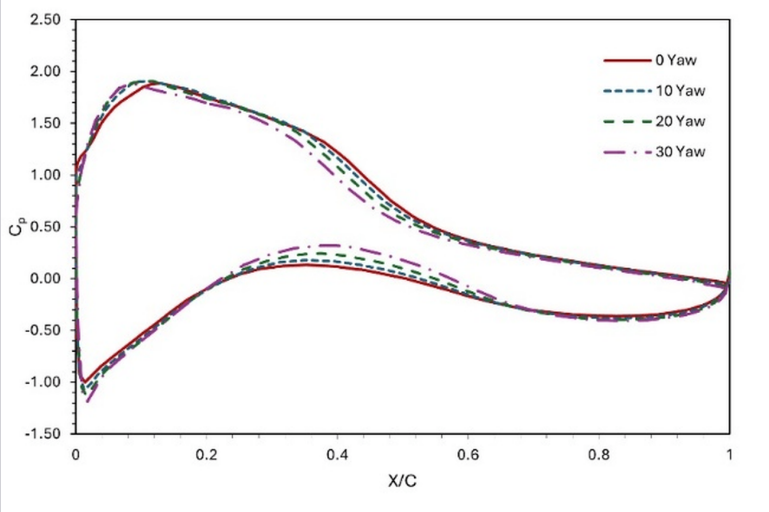

Figure 6. C_p at 60% span at different yaw angles.

The wake profiles extracted at 2D downstream of the rotor, where D is the rotor diameter, reveal the strong influence of yaw misalignment on the wake profiles in the near-wake region (See Fig. 7). For the aligned case (yaw = 0°), the wake exhibits a symmetric double-Gaussian shape with two pronounced velocity deficits corresponding to the tip-shear regions, and a slight recovery near the centreline due to hub not being included in the analysis. As yaw angle increases, the wake becomes increasingly asymmetric and laterally displaced, due to the action of the counter-rotating vortex pair generated under yawed inflow. This deflection shifts the low-momentum wake laterally away from the rotor axis, mixing with higher-speed free-stream air. These trends confirm the impact of yaw misalignment on the wake.

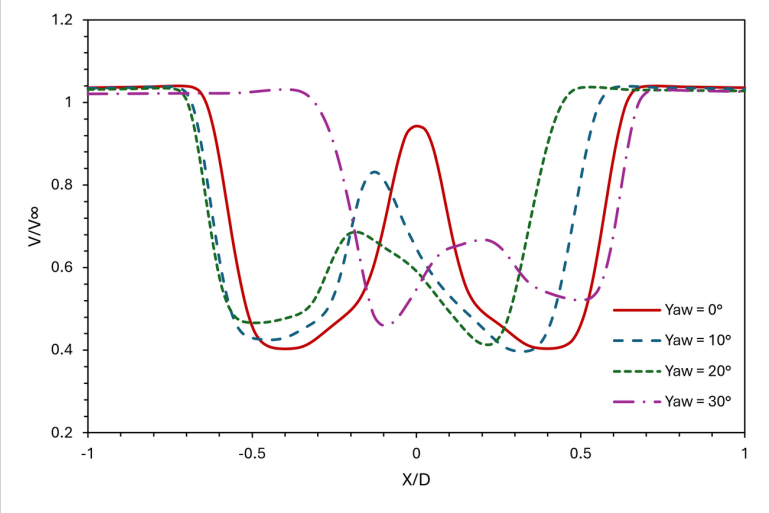

Figure 7. Normalised velocity profiles extracted at 2D downstream of the rotor at different yaw angles.

The deformation of the blade subject to different yaw conditions is depicted in Table 1 and Fig. 8. Table 1 uses a coloured mapping to emphasise these cases with the maximum displacement of each blade. As expected, the largest point of deflection occurs at the tip of the blade, however notably in Table 1 the degree to which the deformation changes between each blade position depends on the angle of yaw. While yaw misalignment introduces greater aerodynamic asymmetry across the rotor, it simultaneously reduces the component of the incoming wind velocity normal to the rotor plane. As the yaw angle increases, the effective axial velocity seen by the rotor decreases approximately in

proportion to the cosine of the yaw angle, thereby reducing the overall aerodynamic loading acting on the blades. At relatively small yaw angles, such as 10°, the reduction in mean aerodynamic loading is limited, while yaw-induced load redistribution can locally increase the loading experienced by individual blades at certain azimuthal positions. As a result, the maximum blade-tip deformation is slightly higher than that of the aligned case, reaching 21.826 mm, corresponding to 1.07% of the blade span. As the yaw angle increases further to 20° and 30°, the reduction in effective axial loading becomes more dominant. Although the aerodynamic loading becomes increasingly asymmetric between the three blades, the overall force acting on the rotor decreases, leading to lower maximum deformations. This explains why the maximum deformation decreases from 21.826 mm at 10° yaw to 20.790 mm at 30° yaw. The smallest deflection among all cases is found to be 17.824 mm (0.874% R) at 30° yaw angle. Deflections are relatively small due to the rigid aluminium blade being modelled; however, the relative differences among blades are more significant and would scale up for flexible blades.

Table 1. Total deformation of each blade at different yaw angles.

Yaw (°)	Blade 1	Blade 2	Blade 3	Unit
0	21.546	21.566	21.570	mm
10	21.826	21.546	20.626	mm
20	21.598	21.017	19.341	mm
30	20.790	19.978	17.824	mm

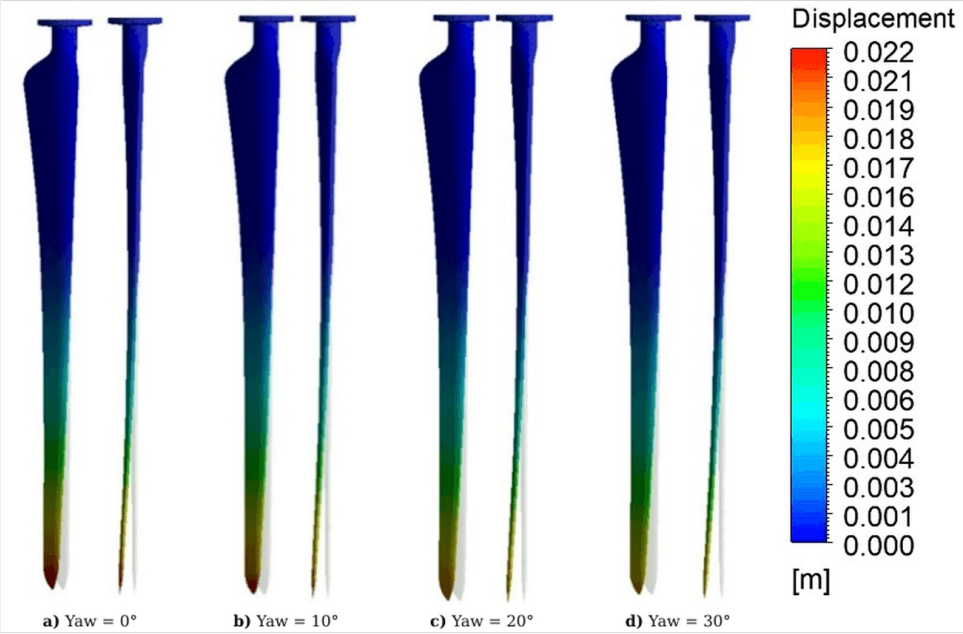

Figure 8. Displacement contours on Blade 3 at different yaw angles.

The stress analysis shows the loading developed in the same locations with similar patterns and comparable magnitudes. Table 2 and Fig. 9 show that the load is not uniformly distributed on each blade of the turbine, with a range of 4.255 MPa at 30° yaw. Furthermore, it is seen that a relatively high yaw angle generally leads to a greater stress range, which indicates a more cyclical nature of loading applied on each blade of the rotor.

Table 2. Equivalent (von Mises) stresses on each blade at different yaw angles.

Yaw (°)	Blade 1	Blade 2	Blade 3	Unit
0	32.040	32.063	32.068	MPa
10	32.365	32.053	30.990	MPa
20	32.125	31.464	29.530	MPa
30	31.230	30.307	27.813	MPa

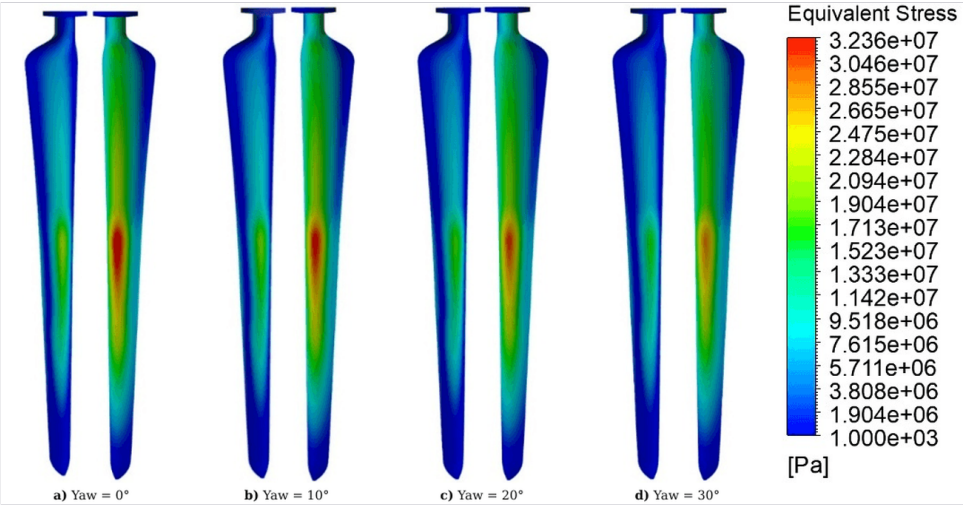

Figure 9. Equivalent (von Mises) stress contours on Blade 3 at different yaw angles.

The aforementioned one-way coupled FSI analysis clearly demonstrates that both blade deformation and aerodynamic loading are asymmetric across the three blades at a given time instant. Consequently, while the blades may exhibit same vibrational amplitudes, their structural oscillations can operate completely out of phase with one another. To replicate this behaviour in the consequent aeroelastic simulations, blade vibrations are set up with the same amplitude but with different inter-blade phase angles. Figure 10 illustrates the aeroelastic setup of a three-bladed wind turbine in which each blade undergoes harmonic vibration with a phase difference of 120°. Figures 10a and 10b present the displacement distribution, with maximum deformation occurring toward the blade tips, representing a typical flapwise-dominated response at a vibration phase angle of 120°. The colour scale highlights that a maximum displacement magnitude of 2% blade span is employed in the aeroelastic simulations. Figure 10c shows the temporal variation of displacement (or response) for the three blades, clearly demonstrating the imposed phase shift, where each blade oscillates with identical amplitude and frequency but offset in time.

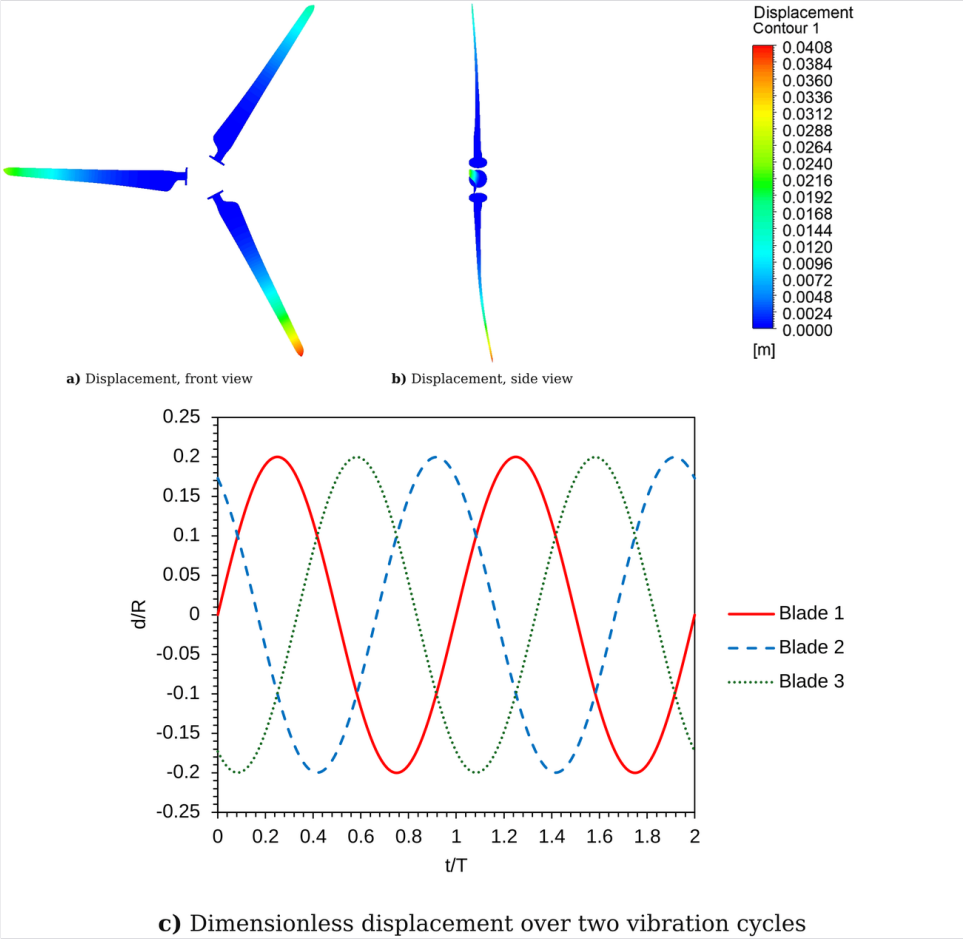

Figure 10. Displacement contours and dimensionless displacement chart over two vibration cycles.

The vibration amplitude of 2% blade span was selected based on two primary considerations. First, the MEXICO rotor employed in the present study is relatively rigid compared to modern utility-scale composite wind turbine blades. Consequently, the structural deformations obtained from the one-way FSI analysis are relatively small, with the maximum blade tip deflection found to be approximately 1.07% of the blade span. Therefore, a prescribed vibration amplitude of 2% span was considered a realistic representation of a small-amplitude structural oscillation.

Second, the selection is consistent with established practices in turbomachinery aeroelastic analyses such as the studies of (Rahmati *et al.* 2013) and (Howison *et al.* 2018), where prescribed vibration amplitudes are typically kept small to characterise aerodynamic damping, unsteady aerodynamic forces, and aeroelastic stability without introducing excessive geometric nonlinearities. The amplitude of 2% span was adopted in the authors' previous aeroelastic investigations (Win Naung *et al.* 2021a). It is acknowledged that the aerodynamic force amplitudes would vary quantitatively if different prescribed vibration amplitudes were selected. However, the primary objective of the study is to investigate the relative influence of yaw misalignment and inter-blade phase differences on aeroelastic behaviour, rather than to establish absolute force levels for a specific vibration amplitude.

Figure 11 illustrates the aerodynamic force responses of the three individual rotor blades over five normalised vibration periods (t/T). The results highlight the coupled effects of the wind turbine's yaw angle (0° and 30°) and the structural vibration phase angle (0° and 120°). In the absence of yaw error (Figs. 11a and 11b), the mean aerodynamic force on each blade remains stable around 585 N with a uniform peak-to-peak amplitude of approximately 110 N. At the phase angle of 0°, the force responses are perfectly synchronised as the blade oscillates in phase, while a 120° structural phase shift sequentially offsets the peak forces of three blades. While the individual blade loading profiles

remain identical in magnitude, the time-delays create a balanced, rotating load distribution across the rotor hub. Introducing a 30° yaw angle (Figs. 11c and 11d) fundamentally disturbs the force responses, due to advancing and retreating effects of the rotor blades cyclical changes in relative wind speed, angle of attack, and structural loads over the blades. Unlike the baseline cases, the force amplitudes are no longer constant with a drop in mean aerodynamic forces. They exhibit alternating high-amplitude and low-amplitude force peaks, associated with the frequency mismatch between the rotational speed and the blade vibration frequency. While a 0° phase synchronises these modulated peaks, they are phase-shifted by 120° when a phase angle of 120° is introduced. Since individual blades experience extreme fatigue cycles, the distributed nature of the peaks could transform localised aerodynamic load variations into complex rotating hub moments.

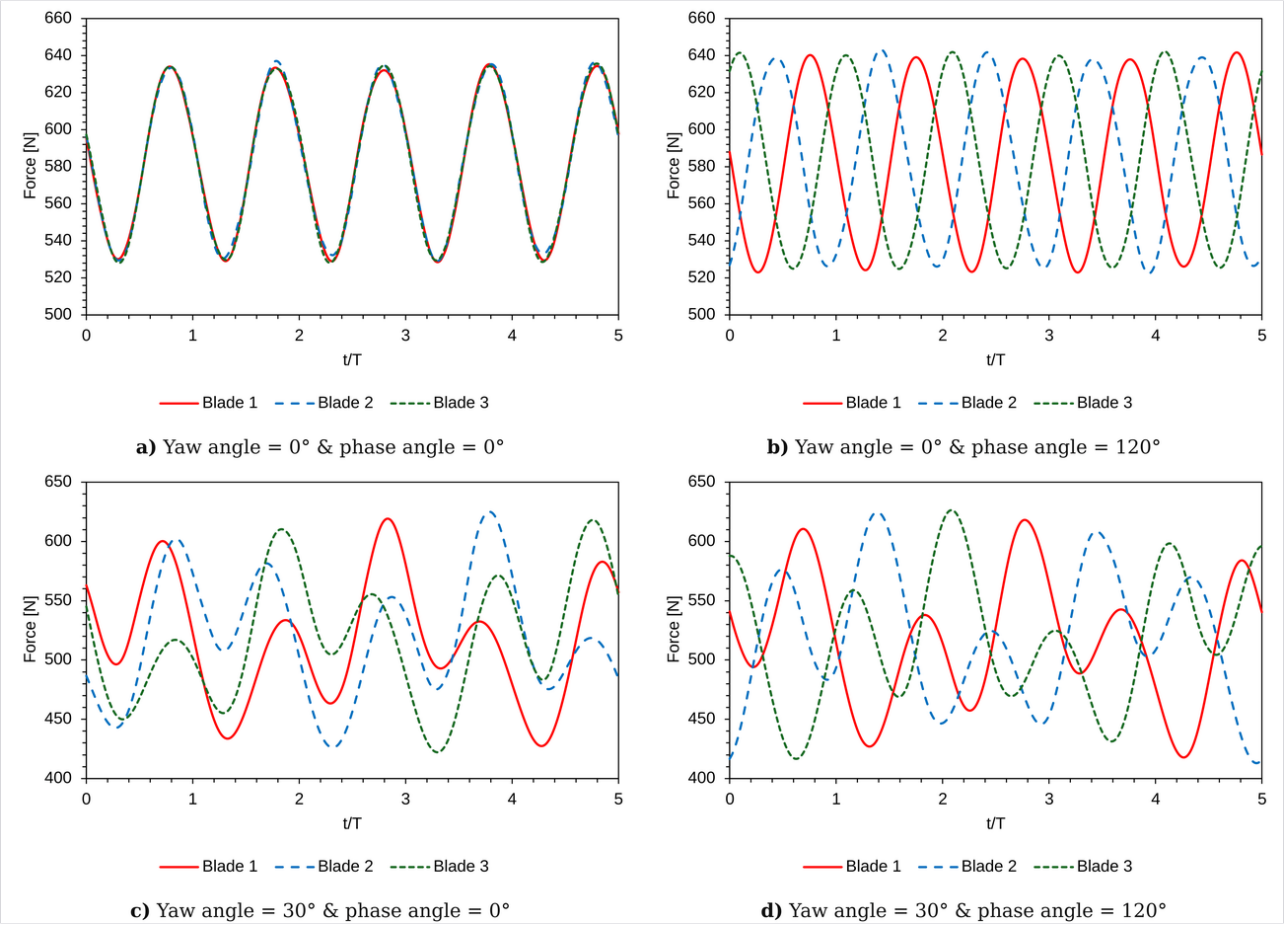

Figure 11. Aerodynamic forces applied over the blades at different yaw angles (0° and 30°) and vibration phase angles (0° and 120°).

Figure 12 displays the wall work density over the three blades at a vibration phage angle of 120°, which directly reflects the energy transfer and aeroelastic stability resulting from the aerodynamic forces. At a 0° yaw angle (Fig. 12a), the work density oscillation indicates an alternating exchange of energy between the fluid and the structure. However, at a 30° yaw angle (Fig. 12b), the amplitude modulation induces periodic fluctuations in the aerodynamic damping margin. While the overall stabilising effect is observed simultaneously across all blades, the yaw-induced modulation could potentially reduce the system's stability margin, leading to the rotor highly vulnerable to severe fatigue and localised forced-vibration instabilities.

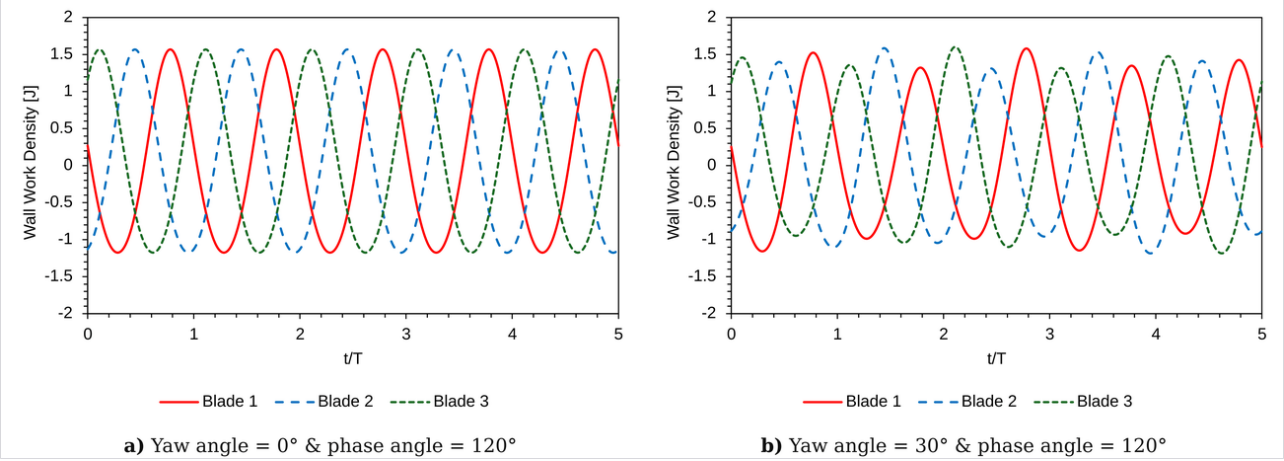

Figure 12. Wall work density applied over the blades at different yaw angles (0° and 30°) at the vibration phase angle of 120°.

Figure 13 presents the spatial distribution of wall work density contours across the pressure and suction sides of the blades under the 30° yawed and 120° phase-shifted condition. The contours reveal that the aeroelastic energy transfer is highly localised and concentrated at the blade tips and along the leading and trailing edges of the outer span with overall stabilising effects. This spatial variation demonstrates that the amplitude modulation and transient stability drop observed in the time-history data are driven primarily by tip-vortex interactions occurring at the outermost sections of the rotor.

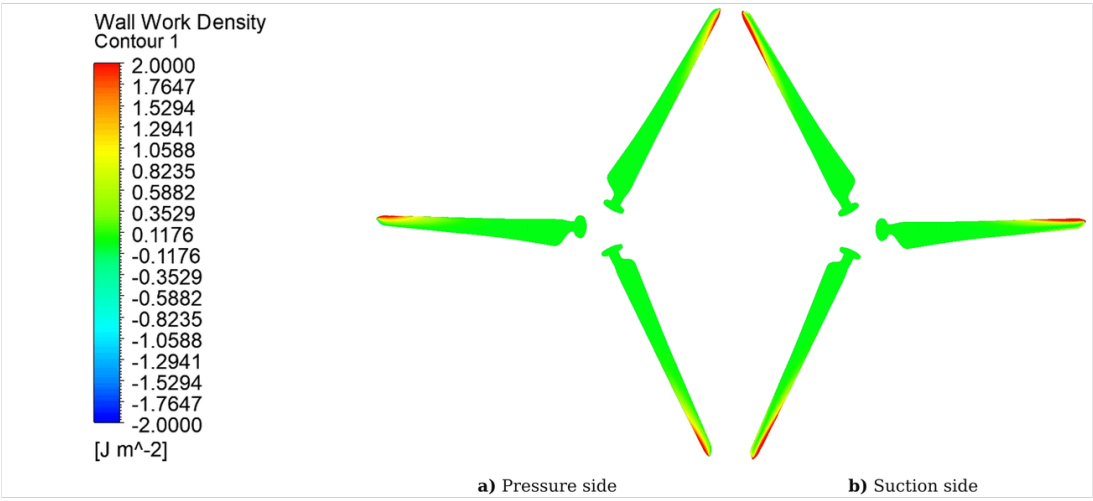

Figure 13. Wall work density contours at the yaw angle of 30° and phase angle of 120°.

As illustrated in Fig. 14, changing the yaw angle appears to not only impact the direction of the wake flow but also affect its velocity magnitudes. The larger yaw angle results in the more significant wake deflection. With increasing yaw angle, the wake is clearly deflected laterally, that indicates the well-known wake skewing effect induced by the misalignment between the rotor plane and the incoming flow. Furthermore, the imposed 120° phase lag in blade vibrations introduces additional unsteadiness into the flow, that can be visible as small-scale fluctuations and irregularities within the wake. These features become more pronounced at higher yaw angles, due to a complex interaction between yaw-induced inflow asymmetry and the structural blade vibration.

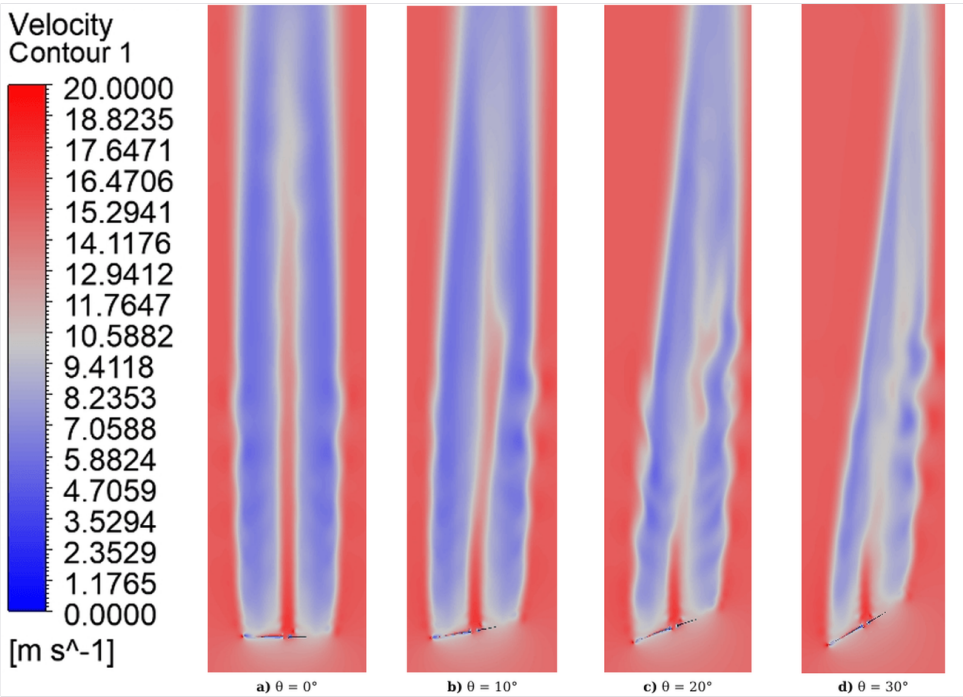

Figure 14. Velocity flow field at different yaw angles (0°, 10°, 20°, and 30°) at the vibration phase angle of 120°.

Figure 15 shows the complex, three-dimensional wake structures through vorticity isosurfaces, coloured by velocity magnitude, under the 30° yawed condition. The isosurfaces capture the generation and downstream evolution of distinct, helical tip vortices shed from the individual blades over 20 and 40 vibration cycles. Due to the 30° yaw angle, the symmetry of the wake breakdown is heavily disrupted. As the wake propagates downstream, the tip vortices experience severe distortion, skewing the helical structure and causing premature vortex pairing and breakdown. As the simulation progresses from 20 cycles to 40 cycles, the continuous injection of vorticity into the skewed flow field significantly extends the downstream wake profile, which reveals a progressively unstable vortex trajectory.

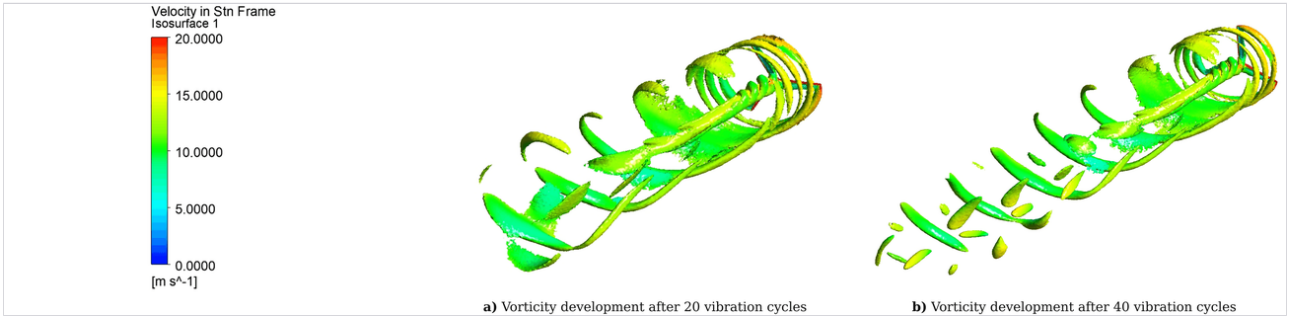

Figure 15. Vorticity iso-surface after 20 and 40 vibration cycles.

5. Conclusions

This study presented a comprehensive aeroelastic analysis of a wind turbine operating under yaw misalignment conditions, combining CFD-based aerodynamic modelling with FEA-based structural assessment. The numerical model was validated against experimental data and benchmark simulations, with excellent agreement among the results. The results demonstrated that yaw misalignment significantly affected the aerodynamic and aeroelastic behaviour of a wind turbine rotor. Increasing yaw angle influenced the blade pressure distribution, with the 30° yaw angle case showing the greatest reduction in pressure coefficients compared with the aligned condition. Yaw

misalignment also caused pronounced wake asymmetry and lateral wake deflection, with wake distortion becoming increasingly severe as yaw angle increased.

The one-way FSI analysis showed that yawed inflow generates non-uniform loading across the blades, resulting in asymmetric deformation and stress distributions. The maximum blade-tip deflection was 21.826 mm (1.07%R) at 10° yaw, while the minimum was 17.824 mm (0.874%R) at 30° yaw. The largest stress variation between blades reached 4.255 MPa at 30° yaw, which indicated greater cyclic loading under higher yaw angles.

Aeroelastic simulations revealed that blade vibration phase differences strongly influence load distribution. Under aligned inflow, all blades experienced similar force responses with a peak-to-peak amplitude of approximately 110 N. In contrast, the 30° yaw condition produced amplitude-modulated aerodynamic forces, reduced mean loading, and more complex rotating hub moments. Wall work density analysis indicated yaw-induced load modulation could potentially reduce the stability margin although the localised stabilising effects were observed in the present study. Furthermore, aeroelastic energy transfer was concentrated near the blade tips and outer-span leading and trailing edges. Wake visualisation confirmed that the combination of 30° yaw and 120° blade phase shift intensified wake unsteadiness, distorted helical tip vortices, and accelerated vortex breakdown, which showed the importance of accounting for coupled aerodynamic-structural interactions under yawed operating conditions.

The proposed numerical framework provides a computationally efficient approach for evaluating the aeroelastic behaviour of wind turbine blades, with detailed identification of deformation, stress distributions, and vibration characteristics while capturing the influence of blade motion on the aerodynamic performance and flow fields. A limitation of the study is that the aeroelastic coupling remains one-way, with the structural deformation prescribed rather than fully interacting with the flow field in real time. Consequently, potential interaction effects between aerodynamic loading and structural response, particularly under highly unsteady operating conditions, may not be fully captured, and a fully coupled FSI approach could be explored in future work. Overall, while yaw misalignment-based strategies appear to offer aerodynamic advantages for wake steering and energy losses, it can potentially introduce significant aeroelastic issues, including increased stress variability, asymmetric deformation, amplified cyclic loading, and intense wake distortion. These factors could reduce turbine lifespan and increase maintenance costs. Therefore, yaw-based control strategies should incorporate aeroelastic constraints and fatigue considerations to ensure long-term reliability of turbine operation. Future works should focus on integrated optimisation frameworks that balance aerodynamic gains with structural durability, supported by long-term fatigue analysis of the turbine.

Declarations

Author contributions. Shine Win Naung: Conceptualization, Methodology, Investigation, Formal analysis, Writing (original draft), Visualization, Validation, Supervision, Project administration, Funding acquisition, Resources, Writing (review and editing), Software. Summer Pimm: Methodology, Investigation, Writing (original draft), Visualization, Validation, Software, Formal analysis. Kai Zhang: Methodology, Investigation, Writing (review and editing). Yufeng Yao: Writing (review and editing), Investigation, Supervision. Jun Yao: Investigation, Writing (review and editing). Mohammad Rahmati: Methodology, Writing (review and editing).

Funding. The authors would like to acknowledge that this research is funded by the Vice Chancellor's Early Career Research (VC ECR) Awarded of the University of the West of England under the grant number of VCECR24-15.

Conflicts of interest. The authors declare that they have no competing interests.

Data availability. The data supporting the findings of this study are available from the corresponding author upon reasonable request.

References

Abdelkhalig, Ashraf; Elgendi, Mahmoud; Selim, Mohamed Y.E. (2022) 'Review on validation techniques of blade element momentum method implemented in wind turbines', *IOP Conference Series: Earth and Environmental Science*, 1074(1), pp. 012008. Available at: https://doi.org/10.1088/1755-1315/1074/1/012008

Arabgolarcheh, Alireza; Jannesarahmadi, Sahar; Benini, Ernesto (2022) 'Modeling of near wake characteristics in floating offshore wind turbines using an actuator line method', *Renewable Energy*, 185, pp. 871-887. Available at: https://doi.org/10.1016/j.renene.2021.12.099

Bechmann, A.; Sørensen, N. N.; Zahle, F. (2011) 'CFD simulations of the MEXICO rotor', *Wind Energy*, 14(5), pp. 677-689. Available at: https://doi.org/10.1002/we.450

Boatto, Umberto; Bonnet, Paul A.; Avallone, Francesco; Ragni, Daniele (2023) 'Assessment of Blade Element Momentum Theory-based engineering models for wind turbine rotors under uniform steady inflow', *Renewable Energy*, 214, pp. 307-317. Available at: https://doi.org/10.1016/j.renene.2023.04.050

Breton, Simon-Philippe; Coton, Frank N.; Moe, Geir (2008) 'A study on rotational effects and different stall delay models using a prescribed wake vortex scheme and NREL phase VI experiment data', *Wind Energy*, 11(5), pp. 459-482. Available at: https://doi.org/10.1002/we.269

Dai, Liping; Zhou, Qiang; Zhang, Yuwen; Yao, Shigang; Kang, Shun; Wang, Xiaodong (2017) 'Analysis of wind turbine blades aeroelastic performance under yaw conditions', *Journal of Wind Engineering and Industrial Aerodynamics*, 171, pp. 273-287. Available at: https://doi.org/10.1016/j.jweia.2017.09.011

Dose, B.; Rahimi, H.; Herráez, I.; Stoevesandt, B.; Peinke, J. (2018) 'Fluid-structure coupled computations of the NREL 5 MW wind turbine by means of CFD', *Renewable Energy*, 129, pp. 591-605. Available at: https://doi.org/10.1016/j.renene.2018.05.064

Dose, B.; Rahimi, H.; Stoevesandt, B.; Peinke, J. (2020) 'Fluid-structure coupled investigations of the NREL 5 MW wind turbine for two downwind configurations', *Renewable Energy*, 146, pp. 1113-1123. Available at: https://doi.org/10.1016/j.renene.2019.06.110

Drofelnik, Jernej; Da Ronch, Andrea; Campobasso, Michele Sergio (2018) 'Harmonic balance Navier-Stokes aerodynamic analysis of horizontal axis wind turbines in yawed wind', *Wind Energy*, 21(7), pp. 515-530. Available at: https://doi.org/10.1002/we.2175

Fernandez, Garbiñe; Usabiaga, Hodei; Vandepitte, Dirk (2018) 'An efficient procedure for the calculation of the stress distribution in a wind turbine blade under aerodynamic loads', *Journal of Wind Engineering and Industrial Aerodynamics*, 172, pp. 42-54. Available at: https://doi.org/10.1016/j.jweia.2017.11.003

Global Wind Energy Council (2025) *Global Wind Report 2025*. Available at: https://www.gwec.net/reports/globalwindreport

Hansen, M. H. (2007) 'Aeroelastic instability problems for wind turbines', *Wind Energy*, 10(6), pp. 551-577. Available at: https://doi.org/10.1002/we.242

Horcas, Sergio González; Debrabandere, François; Tartinville, Benoît; Hirsch, Charles; Coussement, Grégory (2017) 'Extension of the Non-Linear Harmonic method for the study of the dynamic aeroelasticity of horizontal axis wind turbines', *Journal of Fluids and Structures*, 73, pp. 100-124. Available at: https://doi.org/10.1016/j.jfluidstructs.2017.06.008

Howison, Jason; Thomas, Jeffrey; Ekici, Kivanc (2018) 'Aeroelastic analysis of a wind turbine blade using the harmonic balance method', *Wind Energy*, 21(4), pp. 226-241. Available at: https://doi.org/10.1002/we.2157

Lee, H.; Sengupta, B.; Araghizadeh, M. S.; Myong, R. S. (2022) 'Review of vortex methods for rotor aerodynamics and wake dynamics', *Advances in Aerodynamics*, 4(1), pp. 20. Available at: https://doi.org/10.1186/s42774-022-00111-3

Menter, F.R.; Kuntz, M.; Langtry, R. (2003) 'Ten Years of Industrial Experience with the SST Turbulence Model', *Proceedings of the Fourth International Symposium on Turbulence, Heat and Mass Transfer*. Available at: https://api.semanticscholar.org/CorpusID:38105247

O'Brien, J.M.; Young, T.M.; O'Mahoney, D.C.; Griffin, P.C. (2017) 'Horizontal axis wind turbine research: A review of commercial CFD, FE codes and experimental practices', *Progress in Aerospace Sciences*, 92, pp. 1-24. Available at: https://doi.org/10.1016/j.paerosci.2017.05.001

Rahmati, M. T.; He, L.; Wang, D. X.; Li, Y. S.; Wells, R. G.; Krishnababu, S. K. (2013) 'Nonlinear Time and Frequency Domain Methods for Multirow Aeromechanical Analysis', *Journal of Turbomachinery*, 136(4). Available at: https://doi.org/10.1115/1.4024899

RenewableUK (2024) *Floating Wind: Anchoring the Next Generation Offshore*. Available at: https://www.renewableuk.com/news-and-resources/publications/floating-wind-anchoring-the-next-generation-offshore/

Rodriguez, Steven N.; Jaworski, Justin W. (2020) 'Strongly-coupled aeroelastic free-vortex wake framework for floating offshore wind turbine rotors. Part 2: Application', *Renewable Energy*, 149, pp. 1018-1031. Available at: https://doi.org/10.1016/j.renene.2019.10.094

Schepers, J.G. et al. (2014) *Final report of IEA Task 29, Mexnext (phase 1): analysis of MEXICO wind tunnel measurements*. ECN, Petten, the Netherlands (ECN-E-07-042). Available at: http://www.ecn.nl/publications/ECN-E--12-004

Shao, Yi-Xiao; Wang, Zhen-Fan; Win Naung, Shine; Zhang, Kai; Yao, Yufeng; Zhou, Dai (2025) 'Towards high-fidelity wind farm layout optimization using polynomial chaos expansion and Kriging model', *Energy*, 338, pp. 138820. Available at: https://doi.org/10.1016/j.energy.2025.138820

Snel, H; Schepers, J G; Montgomerie, B (2007) 'The MEXICO project (Model Experiments in Controlled Conditions): The database and first results of data processing and interpretation', *Journal of Physics: Conference Series*, 75, pp. 012014. Available at: https://doi.org/10.1088/1742-6596/75/1/012014

Tu, Yu; Zhang, Kai; Han, Zhaolong; Zhou, Dai; Bilgen, Onur (2023) 'Aerodynamic characterization of two tandem wind turbines under yaw misalignment control using actuator line model', *Ocean Engineering*, 281, pp. 114992. Available at: https://doi.org/10.1016/j.oceaneng.2023.114992

Wang, Lin; Liu, Xiongwei; Renevier, Nathalie; Stables, Matthew; Hall, George M. (2014) 'Nonlinear aeroelastic modelling for wind turbine blades based on blade element momentum theory and geometrically exact beam theory', *Energy*, 76, pp. 487-501. Available at: https://doi.org/10.1016/j.energy.2014.08.046

Wang, Lin; Quant, Robin; Kolios, Athanasios (2016) 'Fluid structure interaction modelling of horizontal-axis wind turbine blades based on CFD and FEA', *Journal of Wind Engineering and Industrial Aerodynamics*, 158, pp. 11-25. Available at: https://doi.org/10.1016/j.jweia.2016.09.006

Wang, Tengyuan; Cai, Chang; Liu, Junbo; Peng, Chaoyi; Wang, Yibo; Sun, Xiangyu; Zhong, Xiaohui; Zhang, Jingjing; Li, Qingan (2024) 'Wake characteristics and vortex structure evolution of floating offshore wind turbine under surge motion', *Energy*, 302, pp. 131788. Available at: https://doi.org/10.1016/j.energy.2024.131788

Win Naung, Shine; Rahmati, Mohammad; Farokhi, Hamed (2021a) 'Aeromechanical Analysis of a Complete Wind Turbine Using Nonlinear Frequency Domain Solution Method', *Journal of Engineering for Gas Turbines and Power*, 143(1). Available at: https://doi.org/10.1115/1.4049206

Win Naung, Shine; Rahmati, Mohammad; Farokhi, Hamed (2021b) 'Direct Numerical Simulation of Interaction between Transient Flow and Blade Structure in a Modern Low-Pressure Turbine', *International Journal of Mechanical Sciences*, 192, pp. 106104. Available at: https://doi.org/10.1016/j.ijmecsci.2020.106104

Win Naung, Shine; Nakhchi, Mahdi Erfanian; Rahmati, Mohammad (2021c) 'High-fidelity CFD simulations of two wind turbines in arrays using nonlinear frequency domain solution method', *Renewable Energy*, 174, pp. 984-1005. Available at: https://doi.org/10.1016/j.renene.2021.04.067

Win Naung, Shine; Rahmati, Mohammad; Farokhi, Hamed (2021d) 'Nonlinear frequency domain solution method for aerodynamic and aeromechanical analysis of wind turbines', *Renewable Energy*, 167, pp. 66-81. Available at: https://doi.org/10.1016/j.renene.2020.11.046

Win Naung, Shine; Kyaw, Myo Tun; Zhang, Kai; Yao, Yufeng; Yao, Jun; Rahmati, Mohammad (2025a) 'Aeroelastic Analysis of a Wind Turbine Operating in the Wakes of an Upstream Wind Turbine', *Proceedings of Global Power & Propulsion Society*. GPPS. Available at: https://doi.org/10.33737/gpps25-tc-244

Win Naung, Shine; Rahmati, Mohammad; Shine, Htet (2025b) 'High-Fidelity Aeroelastic Analysis of a Wind Turbine Using a Nonlinear Frequency-Domain Solution Method', *Energies*, 18(5), pp. 1195. Available at: https://doi.org/10.3390/en18051195

Yang, Jian; Fang, Lingqi; Song, Dongran; Su, Mei; Yang, Xuebing; Huang, Lingxiang; Joo, Young Hoon (2021) 'Review of control strategy of large horizontal-axis wind turbines yaw system', *Wind Energy*, 24(2), pp. 97-115. Available at: https://doi.org/10.1002/we.2564

Zhang, Wenzhe; Calderon-Sanchez, Javier; Duque, Daniel; Souto-Iglesias, Antonio (2024) 'Computational Fluid Dynamics (CFD) applications in Floating Offshore Wind Turbine (FOWT) dynamics: A review', *Applied Ocean Research*, 150, pp. 104075. Available at: https://doi.org/10.1016/j.apor.2024.104075

HOW TO CITE THIS PAPER

Win Naung, S., Pimm, S., Zhang, K., Yao, Y., Yao, J. and Rahmati, M. (2026). Numerical investigation of the aeroelastic performance of a wind turbine operating under yaw misalignment. In: *Proceedings of the 22nd International Conference on Sustainable Energy Technologies (SET2026)*, Kuala Lumpur, Malaysia, 13 to 15 August 2026. Caravel Press, pp. 343–360. ISBN 978-1-995850-00-9. ISSN 2978-4387. https://doi.org/10.65582/set.2026.030

COPYRIGHT AND LICENCE

© 2026 The Author(s). This is an open access paper distributed under the terms of the Creative Commons Attribution (CC BY 4.0) licence, which permits unrestricted use, distribution and reproduction in any medium, provided the original work is properly cited.

WSSET World Society of Sustainable Energy Technologies Organised by the World Society of Sustainable Energy Technologies. Published by Caravel Press.